Drop expansion driven by bubbling on microscale patterned substrates under low air pressure

Jiangen Zheng[a], Jiayan Li[a], Yingzhou Huang[a,*], Shuxia Wang[a], Guo Chen[a,*], Lei Xu[b]

[a] Chongqing Key Laboratory of Soft Condensed Matter Physics and Smart Materials, College of Physics, Chongqing University, Chongqing 400044, People's Republic of China
[b] Department of Physics, The Chinese University of Hong Kong, Hong Kong, China

HIGHLIGHTS

- The two kinds of drop behavior under low air pressure were investigated.
- The critical air pressure for drop expansion was analyzed and experimentally verified.
- The bubbling mechanism on microscale patterned substrates was illustrated.
- Two stages of drop expansion driven by bubbling was demonstrated.

GRAPHICAL ABSTRACT
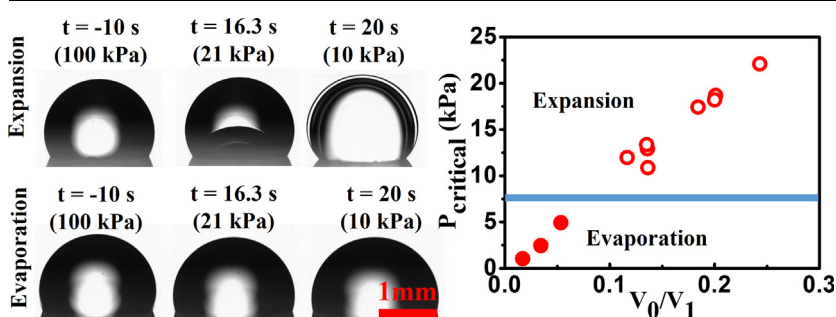
ARTICLE INFO

ABSTRACT

The growth of bubbles has been extensively studied for decades. However, the bubbling inside a single drop on complex surfaces and its subsequent effects on drop are not well understood yet. A systematical investigating of bubbling mechanism in drops on customized microscale pore-patterned surfaces is presented, and the results demonstrate that drop behaviors can be controlled under low air pressure. As the pressure decreases, the drop behaves via two approaches, depending on the competition between the critical chamber pressure and the lower limit of pressure. When the former one is higher, drop prefers to expand, otherwise, evaporation occurs. Further studies suggest that the drop expansion consists of two stages: pinning mode and pinning to depinning transition. This work provides new insights in understanding of bubbling physics on complex patterned substrates, opens a general route for the controlling of drop behaviors under low air pressure, and can also find potential applications in optimization design for self-cleaning patterned surface.

1. Introduction

Bubbling, whether it occurs inside air, liquid, or even solid, is a common phenomenon in nature [1–6]. To our knowledge, the studies on bubbling can be traced back to 19th century [7–9]. Bubbling is also important technologically in medicine and in industry, widely appearing in drug delivery [10,11], *in situ* non-invasive destruction of damaged tissues or obstructions [12,13], isolating object from erosion [14], and noise absorption [15]. Therefore, it is of great significance to understand the physical mechanism of bubbling and its consequent effects.

The bubbling process is usually started from a nucleation event and can be triggered by a number of ways, such as pressure reduction [16–18], acoustic shock [19–23], catalytic decomposition [24], electric
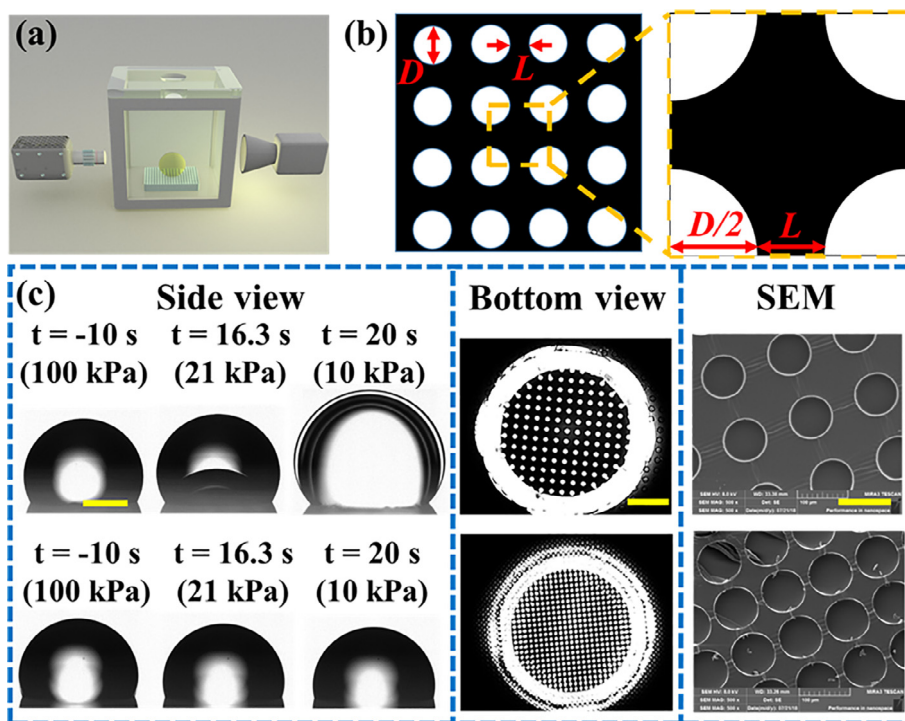

Fig. 1. (a) Diagram of the experimental setup. A drop is placed on a pore-patterned PDMS substrate inside a transparent vacuum chamber. (b) A cartoon illustrating the surface appearance of the substrate. Black and white indicate the solid and hole part respectively. D is the diameter of the hole and L is the space between two neighbor holes. The height of the hole is H, which is not shown here. The magnified image indicated by the yellow dashed box shows the basic unit of substrate and can help to calculate the solid fraction. (c) Side-view images show two different kinds of drop behavior on pore-patterned substrates under low pressure. A drop can either expand (Top) or evaporate (Bottom). The corresponding bottom-view images before depressurization indicate that air pockets can be entrapped inside the pores below the water drop for both cases. SEM-view images show the pore sizes of the corresponding surfaces. Scale bars are 1 mm, 500 μm, and 100 μm, respectively, from left to right. (For interpretation of the references to colour in this figure legend, the reader is referred to the web version of this article.)

heating [25], and light heating [26–28]. Among them, air bubble inside bulk water growing on a solid surface in response to a pressure reduction is the one of the most widely used research approach [16]. The growth of the bubbles in such situation is found to be symmetrical in morphology and experiences three stages: the floating stage with a constant radius, the transition stage with a significant change in both contact angle and bubble radius, and the expansion stage with a constant contact angle [16]. However, the thorough understanding of bubbling inside a single drop on complex surfaces is still lacking, let alone the studies of drop behaviors associated with bubbling. Meanwhile, bubbles in real environments or industries tend to be created and attached to surfaces that are not completely smooth or even rough [19,29,30], which makes the study of bubbling in complex environment have general and practical significance.

Inspired by the research findings that a sessile drop on a suitably-designed patterned surface can achieve the Cassie–Baxter state, or a metastable state [17], and air pockets are trapped below the drop in both states. These air pockets serve as nuclei, and once the atmospheric pressure is reduced sufficiently, they will expand to coalesce with the neighbors, and yield a big growing bubble, resulting in the expansion of the drop [17]. In this work, we thus place drops on customized microscale pore-patterned surfaces under low atmospheric pressure. We notice that not every drop expands unless the corresponding critical pressure surpasses the lower limit of chamber pressure. When drop expansion occurs, its morphology change is asymmetric and it goes through two stages: pinning stage and pinning to depinning transition. Our experiments demonstrate that the special surface micro-structures on patterned surface bring fundamentally different bubbling physics and enrich the consequent drop behaviors. A suitably customized surface can be used to promote or prevent the yield of bubbles, and thus further manipulates drop behaviors to realize either expansion or evaporation. Furthermore, the observation of rapid movement of base

diameter during pining to depinning transition may provide inspiration for patterned surface design to strength the effect of drop sliding on hydrophobic surface. This study provides a new approach to study drop expansion driven by bubbling, generalizes the understanding of bubbling and associated drop behaviors to a more complex system, and can also be applied to the optimization design for self-cleaning hydrophobic surface.

2. Experiments and methods

2.1. Tested surfaces

Different microscale pore-patterned PDMS surfaces with varying diameters and spaces were used in our experiments. Firstly, the pillar-patterned mold was fabricated based on standard UV photolithography (URE-2000/35, China) and dry-etching on a clean silicon wafer. The height of the pillar was ~23 μm by precisely adjusting the dry-etching process. After that, the silicon mould was placed on the heating plate (IKA C-MAG HP7; Germany) baked for 12 h at 120 °C. Then, the samples with micro-pore arrays were obtained by reverse-mould with PDMS through micro-pillar arrays silicon template. Polydimethylsiloxane (PDMS, SYLGARD 184; America) base mixed with curing agent at a ratio of 10:1 was poured over the patterned region of the mold and placed in the vacuum oven for de-gassing, and placed on the drying oven (DZF 6020; China) at 70 °C for 2 h. After curing, the pore-patterned PDMS layer was gently peeled off in ethanol solution.

2.2. Surface characterization

The PDMS surfaces were properly cut and treated by gold spraying process (SBC-12 type ion sputter, China) for 90 s, and then measured by

scanning electron microscope (SEM, Tescan Mira3 LMH; Czech). The pore sizes for different surfaces varied from 20 μm to 80 μm in diameter and 10 μm to 50 μm in spacing.

2.3. Contact angle and sagging depth measurement

The drop was firstly dyed by Rhodamine 6G, and then we used confocal microscope (Leica TCS SP8; Germany) to capture the contact angle in the advanced state on the pore's sidewall and the sagging depth of drop.

2.4. Experimental procedure and apparatus

The entire experiment was carried out in a transparent PMMA chamber as shown in Fig. 1a. The chamber was connected to a vacuum pump (2XZ-2 rotary vane vacuum pump; China) to realize a low inside air pressure. We measured the real time pressure values with a vacuum gauge (BOOST.PLD.0201; China) and the low limit of pressure in our experiment is 7.5 kPa. We used a high-speed camera (Phantom V7.3; Ametek, USA) equipped with a 5× lens (M Plan APO 5X; Japan) to capture the drop placed on the pore-patterned PDMS surface. The bottom view images were recorded by mounted the transparent PMMA cavity on an inverted microscope (Olympus IX73; Japan) with a 10× objective (Olympus M Plan FLN 10X/0.3, Japan). During each test, 4 μL deionized water were used extracted with a pipette (Eppendorf Research plus 0.2–10 μL; Germany) and placed on a substrate inside the transparent chamber. Then, we connected the chamber with the vacuum pump and sealed with vacuum oil at the joint.

3. Results and discussion

3.1. Two kinds of drop behavior under low air pressure

In this experiment, we place a de-ionized water drop with diameter $D_0 = 2.2 \pm 0.1$ mm on a microscale pore-patterned poly-dimethylsiloxane (PDMS) substrate inside a transparent vacuum chamber, as shown in Fig. 1a. The pressure, $P_{chamber}$, could be varied between 7.5 and 100 kPa (100 kPa is normal atmospheric pressure). The subsequent evolution of drop is recorded by a Phantom V7.3 high-speed video camera at a frame rate of 500 fps. Different PDMS substrates with different pore sizes are fabricated by mold-based UV optical lithography. The pores on these substrates have the same height H (23 μm), but different diameters D (20, 40, 60, 70, and 80 μm) and spaces between them L (10, 20, 30, 40, and 50 μm), as illustrated by Fig. 1b. The solid fraction φ is defined as the area ratio between the solid part and the entire substrate. Specifically, it can be calculated by dividing the area of black part by the total area as shown in Fig. 1b, which gives $\varphi = 1 - \frac{\pi D^2}{4(D+L)^2}$.

In order to make sure that our results are generally valid, the experiment with identical conditions were repeated at least five times and we replaced the substrate with a fresh and identical one after each measurement to avoid contamination of the substrate due to the residue left by the previous drop. All experiments exhibit consistent behaviors that demonstrate the robustness of our finding.

Fig. 1c shows two kinds of phenomena when a drop is placed on a microscale patterned substrate in the vacuum chamber with gradually decreasing pressure (see the movie, S-1, in the Supplemental Material). The side-view images on the top row show that an air bubble forms inside the drop on the substrate with size of $L = 50$ μm, $D = 80$ μm and it expands rapidly to enlarge the volume of the drop due to the increasing pressure difference between the inside and outside of the drop. However, when the drop is placed on some special substrates, for example, the substrate with size of $L = 10$ μm, $D = 80$ μm, the expansion of drop disappears completely and its volume decreases slowly due to continuous evaporation, as illustrated by snapshots on the

second row. The corresponding SEM images can confirm the information of dimensional parameters for these two substrates. The two cases of drops have also been checked from bottom before depressurization, and the images in Fig. 1c clearly demonstrate that air pockets can be trapped inside the pores below the water drop for both substrates.
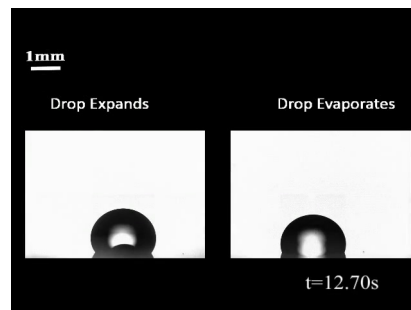
Video S1.

3.2. Bubbling mechanism on pore-patterned surfaces

Why are the air pockets in the second case confined inside the pores all the time when the pressure of chamber decreases, instead of expanding and connecting with each other to make a growing air bubble? We propose an explanation similar to prediction of an ultimate stable superhydrophobic state submerged underwater [17,31]. When a drop is placed on a pore-patterned substrate, a meniscus of liquid may be pinned at the top corner of each hole with a contact angle of θ, leading to the appearance of Cassie–Baxter state, as illustrated by the black dashed curve, state II, in Fig. 2a. Under various conditions such as decreased solid fraction, the meniscus may depin from the top corner and slide down the wall slightly, resulting in the metastable state I in Fig. 2a. The contact angle now is in the advanced state on the pore's sidewall and denoted by θ_a, which is $110 \pm 3°$ and can be experimentally measured by Confocal microscopy (see Fig. 2b inset). The sagging depth, h^*, varying from 0 to 15 μm for different pore sizes on the substrate, can also be measured by Confocal microscopy, as shown in Fig. 2b. When $h^* = 0$, the drop is in state II. Without losing generality, we assume that the initial system is in a metastable state (state I). With the decreasing of pressure in vacuum chamber, the entrapped gas expands and pushes the liquid meniscus upwards to form a dome-shape cap. The edge of bubble travels a horizontal distance x on the solid part of the substrate at angle of θ_r, here θ_r is the receding angle on the flat PDMS surface and has a typical value of $94 \pm 2°$. Once the bubbles reach their neighbors, Coalescence occurs to form a greater bubble, which expands the liquid drop further. Therefore, the critical case where no drop expansion occurs is that the bubble can only reach the state III at which $x = \frac{L}{2}$. The corresponding critical pressure of vacuum chamber is defined as $P_{critical}$.

For both the initial state I and the expansion state III, the pressure difference across the liquid–air interfaces is balanced by the Laplace pressure, i.e.,

$$P_{G,0} + P_{V,0} - P_{L,0} = \gamma_{LG}\kappa_0 \tag{1}$$

$$P_{G,1} + P_{V,1} - P_{L,1} = \gamma_{LG}\kappa_1 \tag{2}$$

Referring to Fig. 2a, the subscripts 0 and 1 denote the state I and III, respectively. γ_{LG} is the liquid–gas interface tension and equals to 72 mN/m for water at 23 °C in this work. κ is the meniscus curvature and $\kappa_0 = \frac{4\cos\theta_a}{D}$, $\kappa_1 = \frac{4\sin\theta_r}{D+L}$. P_G, P_V, and P_L are the pressures of entrapped air, vapor, and liquid respectively. The liquid pressure is mainly controlled by chamber pressure, Laplace pressure and water height (h_w) with respect to the substrate $P_L = P_{chamber} + \frac{2\gamma_{LG}}{R_0} + \rho g h_w$. Here ρ and g are water density and the gravitational acceleration, and R_0 is the radius of the drop. In our experiment, the typical R_0 and h_w are 1.5 mm and 3 mm respectively, leading to $\frac{2\gamma_{LG}}{R_0}\sim$ 0.1 kPa and $\rho g h_w\sim$ 0.03 kPa,
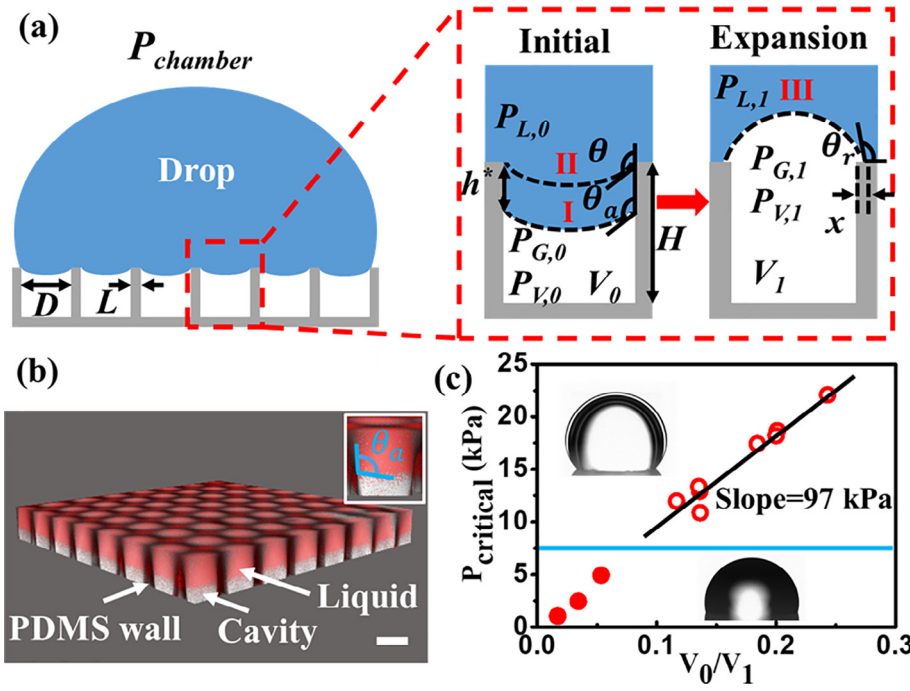
(a)

(b)

(c)

Fig. 2. (a) Cartoon picture (drawn not to scale) illustrating the detailed parameters of a water drop on a patterned substrate. The magnified image indicated by red dashed box show the stable initial and expansion states of liquid–gas interface and cavity morphology under reduced chamber pressure. In initial, the drop can be in a metastable state with a sagging depth of h^* (I) or in a Cassie–Baxter state (II). The critical expansion state (III) when no coalescence of bubbles occurs. (b) The 3-D reconstructed confocal image showing the metastable state of drop on pore-patterned substrate. The white arrows indicate the PDMS wall, cavity, and liquid (dyed by Rhodamine 6G) respectively. Scale bar: 10 μm. The inset shows the advancing contact angle on the pore's sidewall, and $\theta_a = 110 \pm 3°$. (c) Plot of critical vacuum pressure ($P_{critical}$) as a function of the reciprocal coefficient of volume expansion of entrapped air from state I to state III $\left(\frac{V_0}{V_1}\right)$. The linear fitting result with a slope of 97 kPa provides experimental evidence for our model. The blue line indicates the lower limit of vacuum chamber pressure in experiment. Drop expansion occurs (indicated by open symbols) when $P_{critical}$ is greater than this minimum value, otherwise, drop expansion is suppressed (illustrated by solid symbols). (For interpretation of the references to colour in this figure legend, the reader is referred to the web version of this article.)
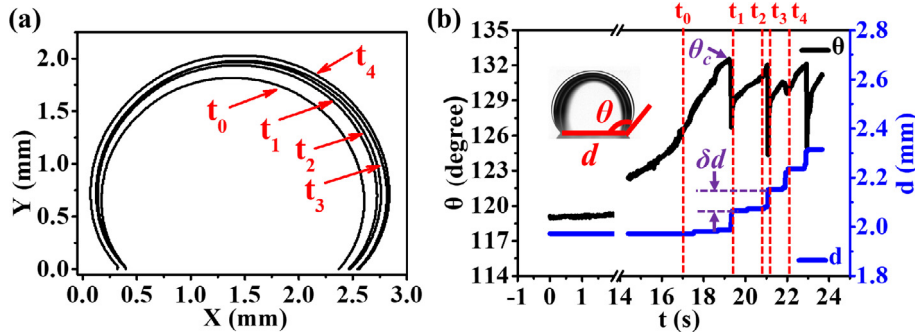
(a)

(b)

Fig. 3. (a) The asymmetric growth of a drop on the patterned substrate under reduced vacuum chamber pressure at five typical moments. Depinning occurs at either the right side of the triple-phase contact angle of drop on substrate (from t_0 to t_1, or from t_2 to t_3), or the left side (from t_3 to t_4). $t_0 = 17.00$ s, $t_1 = 19.34$ s, $t_2 = 20.96$ s, $t_3 = 21.10$ s and $t_4 = 22.10$ s. (b) Corresponding plots of contact angle on the right side of drop, θ, and the base diameter of the triple-phase contact line, d, as a function of time. θ_c is the threshold contact angle just before the pinning to depinning transition. δd indicates the increase of base diameter between two adjacent depinning events (e.g., from t_1 to t_3).

which are both negligible compared with the first term. Thus, at the initial state I, $P_{L,0} = P_{chamber,0} = 100$ kPa, and at the critical expansion state III, $P_{L,1} = P_{critical}$. It's reasonable to assume the expansion of bubble in each cavity is an isothermal process and the vapor saturation condition always holds. According to the ideal gas law, we have $P_{G,0}V_0 = P_{G,1}V_1$. Here, $V_0 = \frac{\pi D^2(H-h^*)}{4} - \frac{\pi D^3}{24\cos^3\theta_a}(3\sin\theta_a - \sin^3\theta_a - 2)$ and $V_1 = \frac{\pi D^2 H}{4} + \frac{\pi(D+L)^3}{24\sin^3\theta_r}(3\cos\theta_r - \cos^3\theta_r + 2)$ are the volume of entrapped air in each cavity at state I and III respectively. The saturated vapor pressure is denoted by P_V^*, which is constant under thermostatic assumption, leading to $P_{V,0} = P_{V,1} = P_V^* = 2.8$ kPa (at 23 °C in experiment) [31]. Finally, on the basis of the above analysis, we get

$$P_{critical} = (\gamma_{LG}\kappa_0 - P_V^* + P_{chamber,0})\frac{V_0}{V_1} + P_V^* - \gamma_{LG}\kappa_1 \quad (3)$$

In Eq. (3), $\gamma_{LG}\kappa_0$, $\gamma_{LG}\kappa_1$ and P_V^* are of the order of a few kPa, while $P_{chamber,0}$ is about 100 kPa and should dominate. So the Eq. (3) could be simplified to a linear relation

$$P_{critical} = P_{chamber,0}\frac{V_0}{V_1} \quad (4)$$

Plugging in the specific parameters of each set of experiments, we obtain the corresponding critical vacuum chamber pressure and show it in Fig. 2c as a function of the reciprocal coefficient of volume expansion of entrapped air. The fitting result indeed reveals such a linear relationship as predicted. The larger volume expansion ratio calls for lower critical chamber pressure. As shown in Fig. 2c, the blue line indicates the minimum pressure limit achievable in our experiment, which is about 7.5 kPa. For cases where the critical pressure $P_{critical}$ is below the pressure limit, drop expansion is suppressed, as illustrated by solid symbols. On the other hand, the open symbols represent the cases with drop expansion. This quantitative agreement provides strong experimental evidence for our model. This finding can be applied to regulation of drop behavior to achieve either expansion or evaporation by using suitably customized surface at reduced air pressure.

3.3. Pinning to depinning transition during drop expansion

More interestingly, we observe that the expansion of drop shows a unique behavior. The external profiles of an expanding drop at five typical moments, $t_0 = 17.00$ s, $t_1 = 19.34$ s, $t_2 = 20.96$ s, $t_3 = 21.10$ s and

$t_4 = 22.10$ s, after the pressure reduction are shown in Fig. 3a. The profile evolution is an asymmetric process. From t_0 to t_1, and from t_2 to t_3, the right end of the triple-phase (liquid–solid–vacuum) contact line shows a sudden increase while the left end remains nearly unchanged. But from t_3 to t_4, the jump of contact line occurs at the left end. We define the base diameter of the triple-phase contact line and the corresponding contact angle on the right side as d and θ, respectively (see Fig. 3b inset), and plot their evolution as a function of time in Fig. 3b main panel. As time goes by, the chamber pressure decreases to reach its lower limit, during which the drop boundary is pinned to the substrate. Therefore, the base diameter of the triple-phase contact line d keeps almost constant (showing a very slow increase) while the right contact angle increases gradually to approach a threshold value, θ_c. At t_1, such a pinning mode changes to a depinning mode with a dramatic decrease of contact angle and a hopping of the base diameter, similar to the depinning during drop evaporation on superhydrophobic surfaces [32]. The increase of base diameter between two adjacent depinning events (e.g., from t_1 to t_3) is defined as δd. δd is composed by two parts: a slowly growth in pinning state (e.g., from t_1 to t_2) and a sharp increase in pinning to depinning transition (e.g., from t_2 to t_3). It should also be noted that the threshold contact angle is significantly smaller near t_4 at which a depinning transition happens, compared with that around t_1 or t_3. The reason is straightforward, the base diameter hopping near t_4 is caused by the depinning of the left end of contact line. At this point, the measured right contact angle has not reached its maximum threshold value yet.

We try to explain the step change behavior of base diameter, by directly observing the evolution of the actual boundary of an expanding drop. The corresponding bottom-view images are shown in Fig. 4a (see the movie, S-2, in the Supplemental Material for a clear demonstration). The three typical moments, t_1, t_2 and t_3, are consistent with the moments shown in Fig. 3 since they come from the same set of experiment. The liquid is squeezed into a thin shell during the drop expansion due to the

gradual increase of the bubble volume inside drop, and its profile is indicated by the black arrow in Fig. 4a. At t_1, the front of liquid just arrives at and is pinned by the periphery of the hole as illustrated by red circles in Fig. 4a. The liquid boundary sweeps the hole along the outer edge of hole slowly. It takes about 1.62 s (from t_1 to t_2) to complete encirclement of the hole. During this period, the base diameter increases at an extremely slow rate, corresponding to the pinning state of drop. Once the encirclement is finished, the liquid front travels forwardly at a velocity which is at least ten times faster than the previous pinning stage, and spends only 0.14 s (from t_2 to t_3) to reach the outer edge of the neighbor hole as indicated by green circles. This rapid change of base diameter corresponding to the pinning to depinning transition. It inspires us to improve the design for patterned hydrophobic surface, such as optimizing the ratio of space and diameter of pores, realizing fast sliding of drop and strengthening the effect of self-clean. Our observation also suggests that the total increase of base diameter during one such event, δd, should match the sum of the diameter of hole and the space between them, i.e., $(D + L)$. Indeed, we find and excellent agreement between δd and $(D + L)$ in experiment, as shown in Fig. 4b.
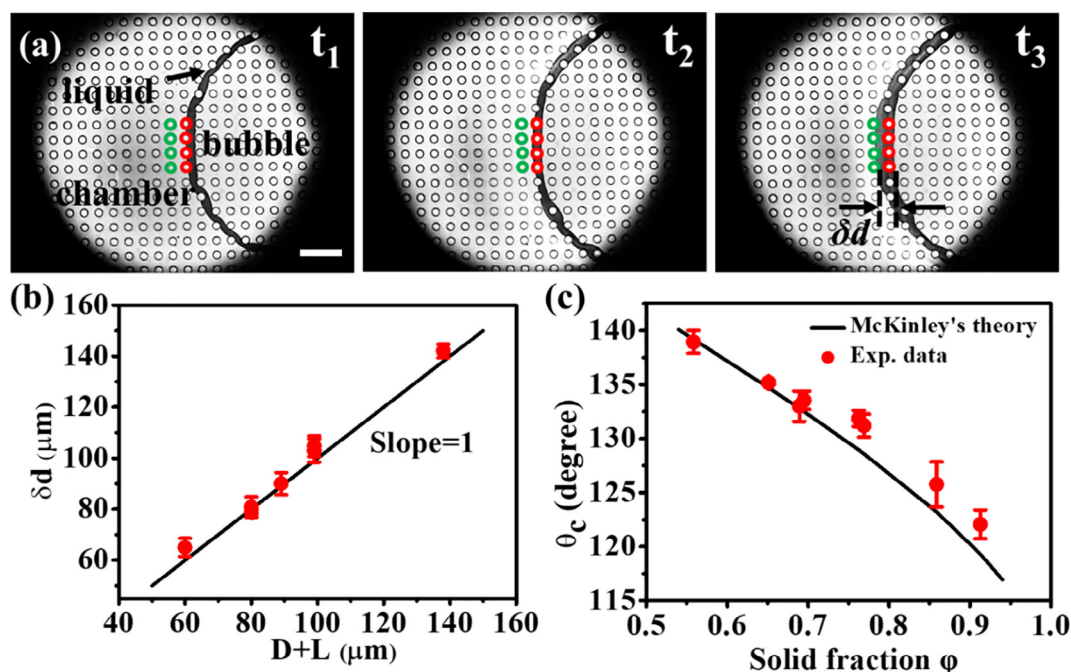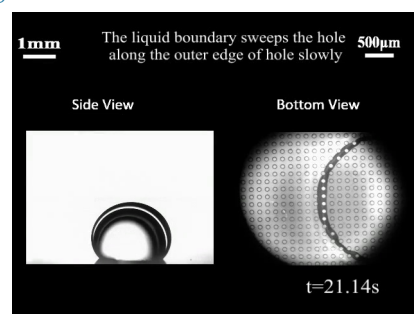

Fig. 4. (a) Bottom view images showing one evolution cycle of the actual boundary of an expanding drop on a pore-patterned PDMS substrate. The three typical moments have one-to-one correspondence with time nodes shown above. $t_1 = 19.34$ s, $t_2 = 20.96$ s, and $t_3 = 21.10$ s. Red and green circles sketch the outlines of the holes involved in this typical evolution cycle. The arrow indicates the liquid shell. Scale bar: 500 μm. (b) Plot of the total increase of base diameter during one evolution cycle, δd, versus the sum of the diameter of hole and the space between them, $(D + L)$. The excellent dependence provides experimental evidence for our model. (c) Plot of threshold contact angle (which is also the advancing contact angle), as a function of solid fraction. Apparently θ_c decrease with φ, indicating lower advancing contact angle is achieved for substrate with higher solid fraction. Red dot: data measured in our experiments; solid line: theoretical prediction by McKinley et al. [33]. This matching also demonstrates the reliability of our model. (For interpretation of the references to colour in this figure legend, the reader is referred to the web version of this article.)

Video S2.

Let's look back to the contact angle on the right side of the drop. It reaches its threshold value, θ_c, at the critical moment of pinning to depinning transition. This θ_c should be consistent with the advancing contact angle of drop on a patterned substrate. We illustrate θ_c as a function of solid fraction φ in Fig. 4c and find θ_c decrease as the increase of φ, possibly due to the higher hydrophobicity under lower solid fraction. Moreover, according to the theoretic model proposed by McKinley and coworkers [33], the apparent advancing contact angle of drop, θ_{adv}^*, on textured surfaces should satisfy the formula: $\cos\theta_{adv}^* = r_\phi \phi_{d,adv}\cos\theta_1 + (1 - \phi_{d,adv})\cos\theta_2$. Where r_ϕ is the roughness of the surface, which is defined as the ratio of the actual surface in contact with the liquid to the projected area of the wetted region. $r_\phi = 1$ since the wetted region is flat in our experiment. $\phi_{d,adv}$ is defined as the differential parameter when the triple-phase contact line is advancing and $\phi_{d,adv} = 1 - \sqrt{1 - \varphi}$. $\theta_1 = 106°$ and $\theta_2 = 180°$ are the equilibrium contact angles on a plat homogeneous solid PDMS and air, respectively. The apparent advancing contact angle curve from McKinley's theory is also plotted in Fig. 4c and it exhibits excellent agreement with our experimental data. This agreement provides experimental evidence for our assumption that θ_c corresponds to the advancing contact angle.

4. Conclusion

In conclusion, we systematically investigate the bubbling process in a drop on varied microscale pore-patterned surfaces and develop a simple model to illustrate the bubbling mechanism. This work generalizes the understanding of bubbling and consequent drop behaviors on complex patterned substrates, and also has several practical advantages and allow many potential applications. First, we demonstrate that the drop behaviors can be manipulated under low air pressure by simply adjusting the structure parameters of patterned surface to reach different critical pressure for bubbling. The drop expansion occurs when the critical pressure surpasses the lower limit of pressure in experiment, otherwise, the drop prefers to maintain its overall appearance and evaporate slowly at reduced pressure environment. This finding can be applied to regulation of drop behavior under low air pressure. Second, we show that the drop expansion contains two processes: pinning mode and pinning to depinning transition. During the pinning mode, the contact angle of drop on substrate grows gradually to reach the apparent advancing contact angle, and the increase of the base diameter of the triple-phase contact line is quite slow due to the pinning of drop by the periphery of the hole. However, in the pinning to depinning transition, completely different behavior emerges: once the encirclement of hole by liquid front is completed, the contact angle decreases sharply while the base diameter jumps suddenly by a rate at least one order of magnitude faster than that in the pinning state. This may have potential applications in optimization design for patterned surface, to strengthen the effect of drop sliding and to enhance the efficiency of self-cleaning hydrophobic surface.

Acknowledgments

References

[1] D. Lohse, Bubble puzzles, Phys. Today 56 (2003) 36–41.

[2] B. Wilco, R.C.A. Veen, T. Van Der, D.L. Tuan, K.G. Keij, I.R. Winkels, V.D.M. Peters, S. Devaraj, J.H. Chao, D. Lohse Snoeijer, Maximal air bubble entrainment at liquid-drop impact, Phys. Rev. Lett. 109 (2012) 264501.

[3] Y.S. Joung, C.R. Buie, Aerosol generation by raindrop impact on soil, Nat. Commun. 6 (2015) 6083.

[4] B.E. Pinchasik, H. Mohwald, A.G. Skirtach, Mimicking bubble use in nature: propulsion of Janus particles due to hydrophobic–hydrophilic interactions, Small 10 (2014) 2670–2677.

[5] T. Luan, F. Meng, P. Tao, W. Shang, J. Wu, C. Song, T. Deng, Bubble-enabled underwater motion of a light-driven motor, Small 15 (2019) 1804959.

[6] P.P. Wang, J.J. Cilliers, S.J. Neethling, P.R. Brito-Parada, The behavior of rising bubbles covered by particles, Chem. Eng. J. 365 (2019) 111–120.

[7] M.N. Iii, Y.T. Didenko, K.S. Suslick, Sonoluminescence temperatures during multi-bubble cavitation, Nature 401 (1999) 772–775.

[8] B.W. Zeff, B. Kleber, J. Fineberg, D.P. Lathrop, Singularity dynamics in curvature collapse and jet eruption on a fluid surface, Nature 403 (2000) 401–404.

[9] D.J. Durian, Foam mechanics at the bubble scale, Phys. Rev. Lett. 75 (1995) 4780.

[10] K.J. Chen, H.F. Liang, H.L. Chen, Y. Wang, P.Y. Cheng, H.L. Liu, Y. Xia, H.W. Sung, A thermoresponsive bubble-generating liposomal system for triggering localized extracellular drug delivery, ACS Nano 7 (2013) 438–446.

[11] K.J. Chen, E.Y. Chaung, S.P. Wey, K.-J. Lin, F. Cheng, C.C. Lin, H.L. Liu, H.W. Tseng, C.P. Liu, M.C. Wei, Hyperthermia-mediated local drug delivery by a bubble-generating liposomal system for tumor-specific chemotherapy, ACS Nano 8 (2014) 5105–5115.

[12] C. Jiménez, G.R. De, A. Aguilera, S. Alonso, A. Cirugeda, J. Benito, R.M. Regojo, R. Aguilar, A. Warlters, R. Gómez, In situ kidney insonation with microbubble contrast agents does not cause renal tissue damage in a porcine model, J. Ultras. Med. 27 (2008) 1607–1615.

[13] R. Vorreuther, R. Corleis, T. Klotz, P. Bernards, U. Engelmann, Impact of shock wave pattern and cavitation bubble size on tissue damage during ureteroscopic electrohydraulic lithotripsy, J. Urol. 153 (1995) 849–853.

[14] A. Philipp, W. Lauterborn, Cavitation erosion by single laser-produced bubbles, J. Fluid Mech. 361 (2000) 75–116.

[15] S.H. Huynh, M. Muradoglu, Y. Yu, T.W. Ng, Captive bubble nucleation, growth, and detachment on plastrons under reduced pressure, Colloids Surf. A Physicochem. Eng. Asp. 509 (2016) 39–47.

[16] L. Jiang, C. Haosheng, Z. Weizheng, W. Bo, S.D. Stoyanov, E.G. Pelan, Growth of bubbles on a solid surface in response to a pressure reduction, Langmuir 30 (2014) 4223–4228.

[17] Y. Xue, P. Lv, L. Ying, Y. Shi, H. Duan, Morphology of gas cavities on patterned hydrophobic surfaces under reduced pressure, Phys. Fluids 27 (2015) 270–280.

[18] P. Lin, F. Wang, L. Liu, Q. He, Characteristics of iron droplet ejection caused by gas bubble bursting under reduced pressure, J. Iron Steel Res. Int. 17 (2010) 7–11.

[19] N. Bremond, M. Arora, C.D. Ohl, D. Lohse, Controlled multibubble surface cavitation, Phys. Rev. Lett. 96 (2006) 224501.

[20] D.Y. Zang, L. Li, W.L. Di, Z.H. Zhang, C.L. Ding, Z. Chen, W. Shen, P.B. Bernard, X.G. Geng, Inducing drop to bubble transformation via resonance in ultrasound, Nat. Commun. 9 (2017) 3546.

[21] T. Lee, H.W. Baac, J.G. Ok, H.S. Youn, L.J. Guo, Nozzle-free liquid microjetting via homogeneous bubble nucleation, Phys. Rev. Appl. 3 (2015) 044007.

[22] A. Volk, C.J. Kähler, Size control of sessile microbubbles for reproducibly driven acoustic streaming, Phys. Rev. Appl. 9 (2018) 054015.

[23] T. Saito, M. Toriu, Effects of a bubble and the surrounding liquid motions on the instantaneous mass transfer across the gas–liquid interface, Chem. Eng. J. 265 (2015) 164–175.

[24] A.A. Solovev, Y. Mei, E. Bermúdez Ureña, G. Huang, O.G. Schmidt, Catalytic microtubular jet engines self-propelled by accumulated gas bubbles, Small 5 (2009) 1688–1692.

[25] Q. Wang, G. Zhang, W. Chao, M. Rong, Y. Wei, The electrically induced bubble behaviors considering different bubble injection directions, Int. J. Heat Mass Transf. 104 (2017) 729–742.

[26] X. Liu, L. Bao, M. Dipalo, F.D. Angelis, X. Zhang, Formation and dissolution of microbubbles on highly-ordered plasmonic nanopillar arrays, Sci. Rep. 5 (2015) 18515.

[27] L. Zhang, J. Xing, X. Wen, J. Chai, S. Wang, Q. Xiong, Plasmonic heating from indium nanoparticles on a floating microporous membrane for enhanced solar seawater desalination, Nanoscale 9 (2017) 12843–12849.

[28] A.L. Klein, W. Bouwhuis, C.W. Visser, H. Lhuissier, C. Sun, J.H. Snoeijer, E. Villermaux, D. Lohse, H. Gelderblom, Drop shaping by laser-pulse impact, Phys. Rev. Appl. 3 (2015) 044018.

[29] P.V.D. Linde, P. Peñas-López, D.V.D. Meer, D. Lohse, H. Gardeniers, D.F. Rivas, Gas bubble evolution on microstructured silicon substrates, Energ. Environ. Sci. 11 (2018) 3452–3462.

[30] Z.D. Huang, M. Su, Q. Yang, Z. Li, S.R. Chen, Y.F. Li, X. Zhou, F.Y. Li, Y.L. Song, A general patterning approach by manipulating the evolution of two-dimensional liquid foams, Nat. Commun. 8 (2017) 14110.

[31] Y. Xiang, S. Huang, P. Lv, Y. Xue, Q. Su, H. Duan, Ultimate stable underwater superhydrophobic state, Phys. Rev. Lett. 119 (2017) 134501.

[32] W. Xu, C.H. Choi, From sticky to slippery droplets: dynamics of contact line depinning on superhydrophobic surfaces, Phys. Rev. Lett. 109 (2012) 024504.

[33] W. Choi, A. Tuteja, J.M. Mabry, R.E. Cohen, G.H. Mckinley, A modified Cassie–Baxter relationship to explain contact angle hysteresis and anisotropy on non-wetting textured surfaces, J. Colloid Interf. Sci. 339 (2009) 208–216.